Ocean Engineering
February 2022, Volume 246 Pages 110438 (12p.)
https://doi.org/10.1016/j.oceaneng.2021.110438
https://archimer.ifremer.fr/doc/00746/85809/

Breaking wave bubble measurements around ship model by optical probe

Khaddaj-Mallat Bachar [1, *], Germain Gregory [1], Billard Jean-Yves [2], Gabillet Céline [2]

[1] Ifremer, Marine Structure Laboratory, 150 Quai Gambetta, 62200 Boulogne sur Mer, France
[2] IRENAV, Ecole Navale, CC 600 - Lanveoc, 29240 Brest Cedex 9, France

* Corresponding author : Khaddaj-Bachar Mallat, email address : bachar.khaddaj-mallat@ensta-paris.fr

Abstract :

The bubble sweep-down phenomenon around oceanographic research vessels generates acoustic disturbances. The phenomenon can be reproduced on a 1/30 scale ship model in a wave and current circulating flume tank taking into account ship motions. Optical probe can then be used to measure locally the size and the velocity of the bubbles generated by breaking waves. A comparison of the obtained results with more classical results obtained from bubble detection by image tracking is discussed. The two methods provide complementary results for bubble characteristics. However, bubble detection by optical probe has the advantage of knowing the bubble position in the three dimensions of space. The overall results of this paper provide new elements for the study and the understanding of the bubble sweep-down phenomenon in addition to previous 2D and 3D studies, where the dynamics of bubble clouds have been characterized.

Highlights

► Bubble sweep-down phenomenon is studied around a 1/30 scale ship model. ► Breaking wave bubble measurements by optical probe were conducted. ► Bubble velocities and diameters were determined. ► Our findings have important implications for marine research vessels.

Keywords : Bubble sweep-down, Breaking wave, Bow wave, Wave and current circulating flume tank, Optical probe, Bubble diameter, Bubble velocity

1. Introduction

The bubble sweep-down phenomenon is a well known phenomenon that affects the acoustic surveys. It has been widely acknowledged for many years [Dalen and Lovik (1981)] and is still a significant issue [Guo et al. (2021),

Mallat et al. (2018a), Mallat et al. (2018b), Delacroix et al. (2016), Shabangu et al. (2014)]. This phenomenon can significantly degrade the transducer performance on oceanographic and research vessels. The causes were identified and they mainly originate from the formation of bubbles by breaking waves coming from the bow entry into the water or from natural wind. These bubbles are trained along the ship hull and under the transducers. These events lead to the disruption of the acoustic signals and may result in a considerable reduction of the ship's productivity. Neither numerical simulations [Li et al. (2016), Moraga et al. (2008), Song et al. (2018)] nor towing tank trials are able to properly address this phenomenon [Johansen et al. (2010)]. Therefore, there is a need in developing models that would enable the prediction of the quantity of bubbles entrapped along the transducers. In addition, the experimental characterization of bubble generation by the breaking bow waves of a ship is scarse. The behaviour of these waves has been studied by [Noblesse et al. (2008), Noblesse et al. (2013), Delhommeau et al. (2009), Delacroix et al. (2016), Mallat et al. (2018b)], who showed their dependency to the bow geometry, the Froude number, the sea states and the ship motions.

Many authors have shown considerable interest in studying and understanding the evolution and dynamics of bubbles generated by breaking waves. Acoustic techniques [Medwin (1977)] have been used to characterize the size and density of small bubbles trapped under the free surface ([Thorpe (1982)], [Akulichev et al. (1986)], [Terrill and Melville (2000)]), or trapped in the wake of the ship ([Abbaszadeh et al. (2020), Trevorrow et al. (1994)], [Vagle and Burch (2005)], [Stanic et al. (2007)]). Measurements are either based on the acoustic scattering volumic cross section of the bubbles or on the acoustic wave attenuation induced when transmitting through a bubbly medium. The latter is a dispersive medium which introduces high variability of the phase velocity near the resonance frequency of the bubbles. This makes the acoustic measurement techniques very sensitive to the acoustic wave frequency and the bubble size repartition. Consequently, acoustic techniques are not the best suited candidate to characterize the sweep-down phenomenon of the bubbles along the ship hull. Interferometric techniques such as Interferometric Particle Imaging (IPI) ([Birvalski et al. (2019)], [Birvalski and van Rijsbergen (2018)]), Interferometric Laser Imaging Technique (ILIT) [Lebrun et al. (2011)], and Digital in-line Holography (DIH) [Lebrun et al. (2010)], can also be considered as potential techniques to measure concentration and size of bubbles in a hydrodynamic flow field.

Moreover, different techniques were used to measure the void fraction in multi-phase flow. Measurements based on the impedance and electrical resistance can be found in the works of [Van der Welle (1985), Ceccio and George (1996), George et al. (2000), York (2001), Holder (2004), Elbing et al. (2008)]. While the use of X-ray imaging in cavitating flows was reported in the works of [Stutz and Legoupil (2003), Coutier-Delgosha et al. (2007), Hassan et al. (2008), Aeschlimann et al. (2011)].

The problem of the characterization of the two-phase flow being extremely difficult to handle properly with the common tools, a specific experimental protocol has been developed in a wave and current circulating flume tank, allowing the 3D visualization and characterization of the bubble sweep-down phenomenon around a specific ship bow [Mallat et al. (2018a)]. In this specific setup, the 3D visualisations carried out have provided insightful informations about 3D trajectories of bubble clouds along the ship hull model. These measurements are complementary with 2D visualisations of the clouds performed by [Mallat et al. (2018b), Delacroix et al. (2016)]. Nevertheless, if 2D and 3D visualisation techniques provide details about the bubble clouds' dynamics, they don't provide any informations about the bubbles size and velocity inside the clouds. For that purpose, based on the results of the 3D study of [Mallat et al. (2018a)], a dual fiber optical probe has been immersed at a position where bubble clouds were observed. The dual fiber optical probe makes it possible to assess, at a given position along the hull of the ship model, the size and streamwise velocity of individual bubbles instead of 3D clouds [Mallat et al. (2018a)].

The first part of this paper presents the experimental set-up allowing the reproduction of the bubble sweep-down phenomenon in a wave and current circulating flume tank. The second part is devoted to the characterization of individual bubbles of the sweep-down phenomenon by optical probe. Diameters and velocities of bubbles generated by breaking waves are identified. The third part focuses on a comparison with a 2D image processing of the bubbles which allows to compute bubble diameters and velocities in a vertical measurement plane. The utilization of both techniques together (local measurement by the optical probe and 2D image processing) allows to access to some particular characteristics of the bubbles, especially their local velocity and the local averaged diameter, which are complementary results of those obtained in [Mallat et al. (2018b),Mallat et al. (2018a)], where 2D and 3D bubble clouds were studied. The final part presents a discussion about the characteristics of the bubbles, expected in real conditions.

2. Experimental set-up

Tests are carried out in the wave and current circulating flume tank of IFREMER in Boulogne-sur-Mer (France) presented schematically in Figure 1. The test section is 18m long x 4m wide x 2m high. Regular waves are generated in direction with the current by a wave generator (Figure 1). The wave frequency range is between 0.5 and 2Hz and the maximum wave height is 300mm with a current speed of 0.8m/s. The resulting reflection coefficient of the wave is lower than 12% for all operating frequencies and amplitudes. The trials can be observed through an observation window of $8 \times 2m^2$ placed on one side of the tank. Wave gauges are placed upstream of the model to measure the free surface elevation. The model is fixed on a motion generator system (hexapod) which reproduces real ship motions.

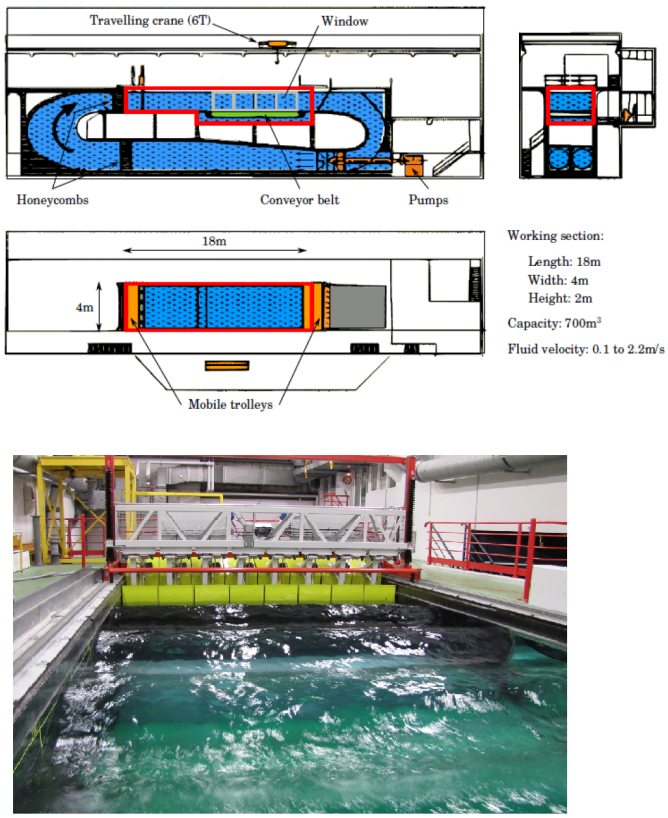

Figure 1: Top: schematic view of the wave and current circulating tank. Bottom: view of the wave generator system with regular waves and current.

A 1/30 scale ship model is considered to study the bubble sweep-down phenomenon observed on the *Pourquoi pas? (Pp?)* during specific acoustic survey. The main conditions during which acoustic perturbations have been encountered were: a ship speed of 8 knots, a wavelength of 109m, a significant wave height H_s of 2.8m and a wave period T_p of 8.4s. The Froude similitude ($Fr^2 = V^2/g.Lpp$, where V is the ship speed, g is the gravity and Lpp is ship length) must be respected to reproduce navigation conditions and sea state encountered during sea surveys. In this study Fr=0.203. The characteristics of the *Pp?* for the present model and its full scales are resumed in the Table 1 where C_B presents the block coefficient of the model. Figure 2 presents the model with side and front views. Trials were conducted on the front part only (1/3 of the model) to avoid perturbations coming from the model stern.

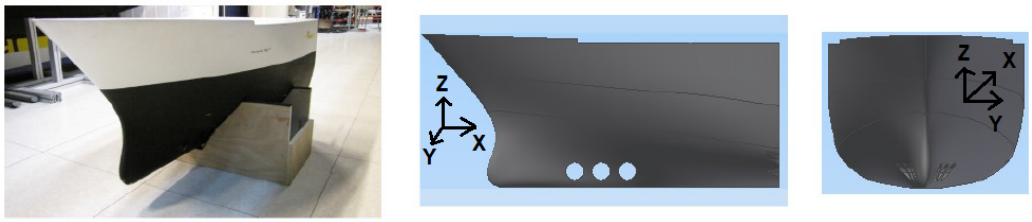

Figure 2: View of the 1/30 scale ship model of Pp?.

The parameters involved in this study are related to the propagation of waves and ship motions. Thus, The bubble dynamics is influenced by the ratio of the inertial force to the surface tension force which is the Weber number $We = \rho L U^2/\sigma$, where ρ is the fluid density, L is the characteristic length and σ is the surface tension. The surface tension effect is relatively more or less significant depending on the characteristics of the wave itself controlled by the dimension of the model. Thus, the Weber number can not be preserved in this study ($We_{model} = 2.5 \times 10^3$; $We_{real} = 2.3 \times 10^5$). On the other hand, it is impossible to comply both Froude and Reynolds similarities preserving the physical characteristics of the fluid. The Reynolds number ($Re = UL_{pp}/\nu$; where ν is the kinematic viscosity) is then largely lower during tank trials comparing to the flow around a full scale vessel by a factor of 100 ($Re_{model} = 2.1 \times 10^6$; $Re_{real} = 3.4 \times 10^8$). The boundary layer very close to the hull is affected by the induced viscous effects and can delay the onset of turbulent flow which is compensated in the flume tank by a strong turbulent intensity of the incoming flow. The shear forces in

the flow close to the model and the amount of air entrainment beneath the surface will be thus significantly reduced. This will be discussed in section 5. To limit the scale effects as much as possible, the model chosen is as large as possible based on the flume tank characteristics (lateral space, wave and current generation).

To reproduce navigation conditions and sea state encountered during the sea survey, the Froude similitude must be respected. Furthermore, the characteristics of the regular waves in the flume tank is calculated to conserve the energy density of irregular waves at sea. The energy density of irregular waves is given by the following expression:

$$E = \rho g m_0 [J/m^2], \text{with } H_s = 4\sqrt{m_0} \tag{1}$$

where H_s is the mean wave height (trough to crest) of the highest third of the waves ($H_1/3$) and m_0 is the zero order moment of the wave energy spectra. For sinusoidal waves:

$$E = \frac{1}{2}\rho g A^2, \text{where A is the amplitude (A = H/2).} \tag{2}$$

To observe energy density conservation, one must write:

$$m_0 = \frac{1}{2}A^2 \tag{3}$$

$$\text{so } A = \sqrt{2}H_s/4 \text{ and H} = \sqrt{2}H_s/2 \tag{4}$$

For $H_s = 2.8m$ the sinusoidal waves with the same energy density will have a wave height of $H = 2.0m$. The period T will be taken equal to T_p. Therefore, the flow velocity in the flume tank is fixed at 0.75m/s and the wave height at 40mm with a frequency of 0.85Hz.

In this study, the imposed motions are determined by means of a numerical model using the computer program FREDYN. A nonlinear strip theory approach is used to compute the hydrodynamic forces acting on the hull. In this head sea configuration, the only significant motions are heave and pitch. Surge motions are here considered insignificant ($< 0,1m$ at full scale). After converting results to the present 1/30 scale ship model by Froude scaling, we finally obtain 20mm for heave and 2° for pitch motions. A key point in the experiments is the synchronization of the waves and motions ([Delacroix et al. (2016)]). To achieve this, hexapod motions have been synchronized

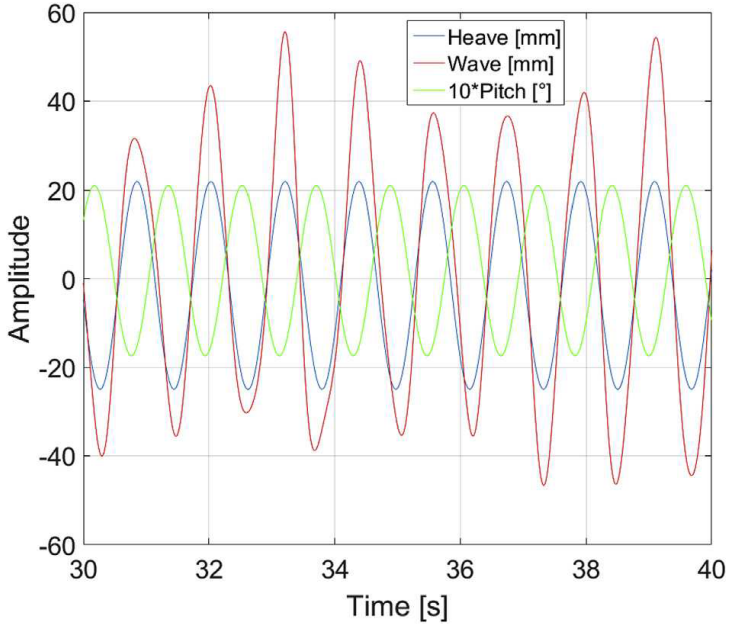

Figure 3: Exemple of imposed ship motions and wave signals on the 1/30 bow ship model.

with the wave and the synchronism has been verified a posteriori (Figure 3).

The flow velocity in the wave and current circulating flume tank is fixed at 0.75m/s and the wave height at 40mm with a frequency of 0.85Hz. In [Mallat et al. (2018a)], for the same operating conditions in the tank, the flow in the vicinity of the bow was characterized by means of Stereo-PIV measurements. For these flow conditions, 3D trajectories of three types of bubble clouds (according to their sizes) were reconstructed. Bubble clouds have been identified by 3D visualization as high reflective areas which correspond to clustering of the bubbles in the three dimensions of space. In the analysis of [Mallat et al. (2018a)], individual bubbles have not been considered.

Figure 4 shows a sketch of the experimental set-up. The instrumentation is composed of a wave probe, a high speed video recording system, as well as an immersed dual fiber optical probe. The wave probe positioned at 3m upstream of the hull is used to determine the wave amplitude throughout the measurement sequence. The interaction between the wave generator and current is the origin of large fluctuations in the amplitude of waves (cf. Figure 5). An average waves' amplitude of 40.7 mm with a standard deviation

	Pourquoi pas?	
	model scale	full scale
$Lpp(m)$	3.13	94
Beam (m)	0.67	20
Draft (m)	0.182	5.46
C_B	0.577	0.577

Table 1: The characteristics of the *Pp?* at model and full scales.

of $\sigma = 10mm$ was measured .

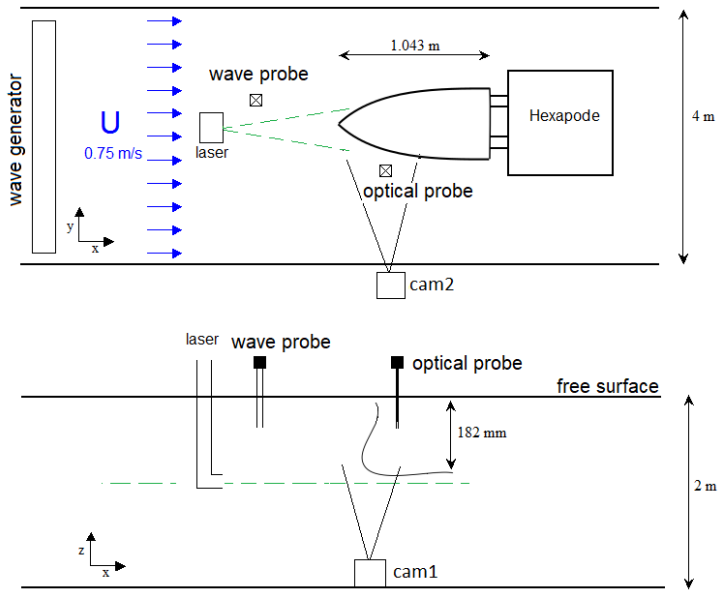

Figure 4: Schematic view of the experimental set-up in the wave and current circulating tank, top and side view.

Furthermore, two cameras are used to visualize the bubble sweep-down phenomenon around the hull. The first camera (cam1) is installed at the bottom of the flume recirculating tank and the second one (cam2) is installed perpendicularly to the first one behind the observation window (Figure 6). The two cameras (Hi-sense CCD camera of $1600 \times 1200 pixels^2$) are synchronized with a frequency rate of 20Hz. It is noteworthy to mention that for simultaneous visualisation of the bubbles when acquiring data from the optical probe, the Nd:YAG laser was not used, as it generates noise on the voltage

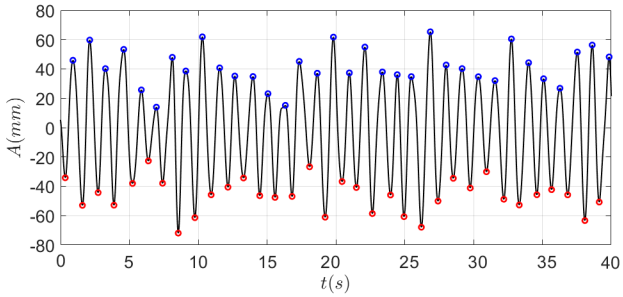

Figure 5: Example of a 40 seconds signal of wave's amplitude.

outputs of the optical probe tips. Thus, the illumination of the probe's area is rather achieved by adding a projector behind the observation window, as shown in Figure 6.

In previous trials, independent with the optical probe trials, pairs of images with time step $dt = 1200\mu s$ are acquired with a PIV camera (Hi-sense CCD camera of $1600 \times 1200 pixels^2$) installed behind the observation window (at same location as cam2 during optical probe measurements) with a frequency of 8.5Hz. For that purpose, a vertical double-cavity Nd:YAG laser, characterized by a wavelength of 532nm, and pulse energy of 200 mJ is localized near the hull (see Figure 7). Raw images in the (x,z) plane obtained from this camera are processed in order to determine, by bubble tracking between consecutive frames, the mean bubble velocity components and the mean bubble size in the vertical plane. A typical raw image corresponding to a bubble cloud passage is shown in Figure 7.

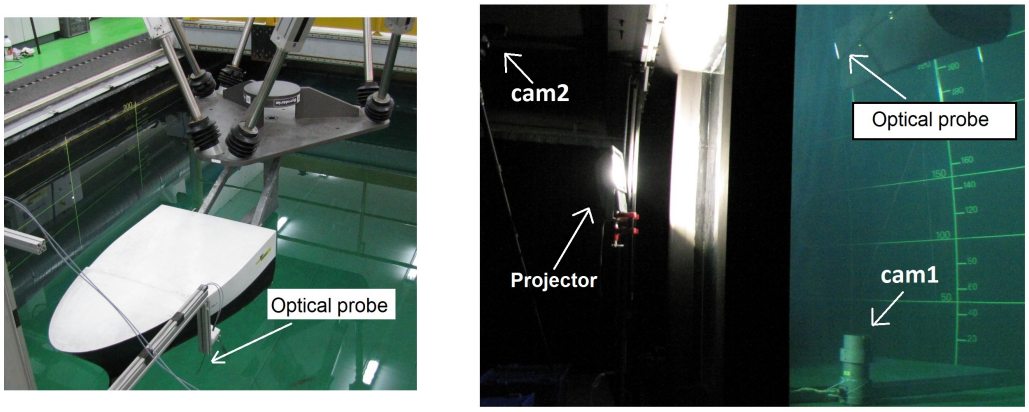

Figure 6: Experimental setup of the bubble measurement study using an optical probe.

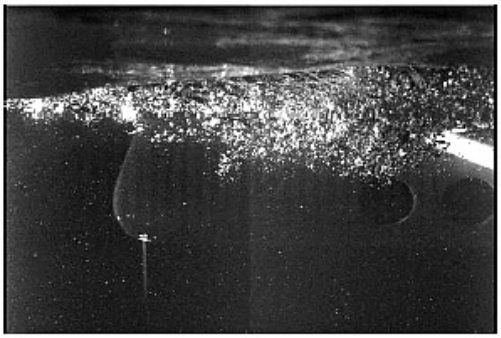

Figure 7: Typical raw image of a bubble cloud acquired with the PIV camera, raw image to be processed to obtain informations on indivual bubbles characteristics.

A dual fiber optical probe and an optoelectronic module manufactured by RBI-Instrumentation are used to detect the instantaneous presence of the gas phase locally near the bow. From these measurements, it is possible to determine the bubbles' velocities and their size. The probe is made of two saphire tips of 30 microns separated in the direction of the current by a distance of 1.15mm in the X direction (Figure 8). Apart from the distance between the tips, the dual probe is the same as the one used in [Mäkiharju et al. (2013)]. The optoelectronic module makes it possible to inject light into the fibers of the probe and to measure the intensity of the light reflected back at the interface of the tips with the surrounding fluid. The optoelectronic module includes a photodetector, associated with an electronic conditioning system

that amplifies and filters the output voltage signal of the photodetector (in volt, V). Due to the difference in the refractive index between water and air, the intensity reflected on the optoelectronic module at the tips varies depending on whether the tip is immersed in water (0 V) or in air (5 V). The measuring system is calibrated by adjusting the gain and offset of the optoelectronic module to achieve a difference in the output voltage in air and water of at least 4V under static conditions ($V_{water} = 0V$; $V_{air} = 4V$ for the upstream tip output and 5,5V for the downstream one). For the trials, the output voltage is recorded with a sampling frequency $f_e = 10kHz$.

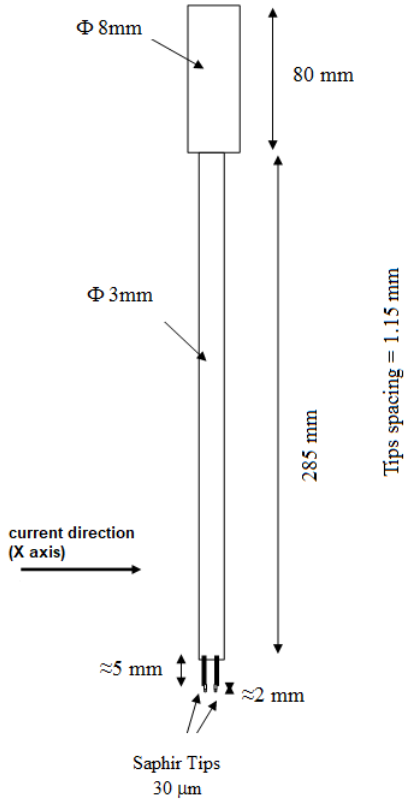

Figure 8: Sketch of the saphire optical probe with double fiber, used to characterize locally the individual bubbles. The distance between the tips is 1.15 mm in the x direction of the flow. The tips extend 5mm from their supports. The main rods of the probe have a diameter of 3mm.

Taking into account the results obtained in previous studies on 3D bubble clouds behavior [Mallat et al. (2018a)], the optical probe is positioned at a

depth of 100 mm (the draft of the model is 182mm) on clouds trajectory. The distance between the model's symmetrical axis and the probe is Y = 250mm and the distance between the tip of the bow and the probe is X = 480mm downstream the tip of the bow. Figure 9 shows a view from cam 1 and cam2 of the model and the probe. The probe is positioned in the (Y,Z) plane with an inclination angle of 20° in respect to the vertical axis. The probe tips are oriented one behind the other along the X axis (the direction of the current). Among the different velocity components of the bubbles, only the main velocity component (oriented in the X direction of the current) is accessible for measurement with the dual optical probe.

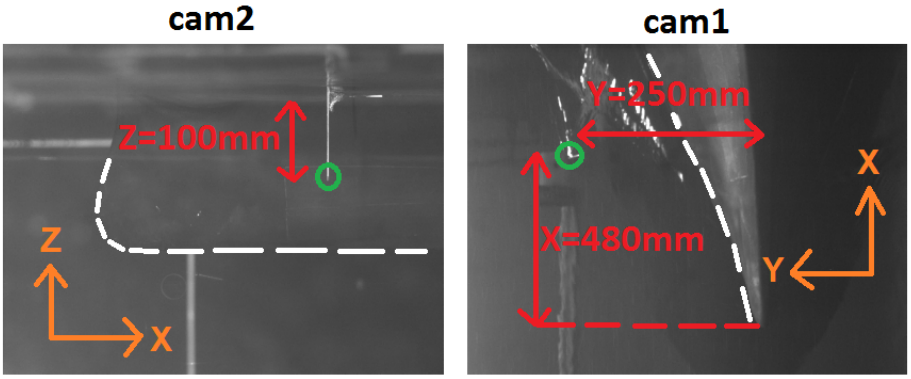

Figure 9: Position of the optical probe around the Pp? model. Green circles correspond to the probe tips location. The dotted line corresponds to the boundary of the model's ship's bow.

Figure 10 and Figure 11 show images of the same time sequence over a wave period taken by the *cam2* behind the window and the *cam1* at the bottom of the wave and current circulating tank. The tip of the optical probe is visible on these Figures (green circle). These pictures allow the visualization of the bubbles cloud passing at the optical probe's location at some instants. Bubbles are identified as bright elements. For the wave period at stake, interactions of the bubble clouds with the probe occurs between instant 6 and instant 11 (cf. Figure 11) which represents a duration of 0.25 s.

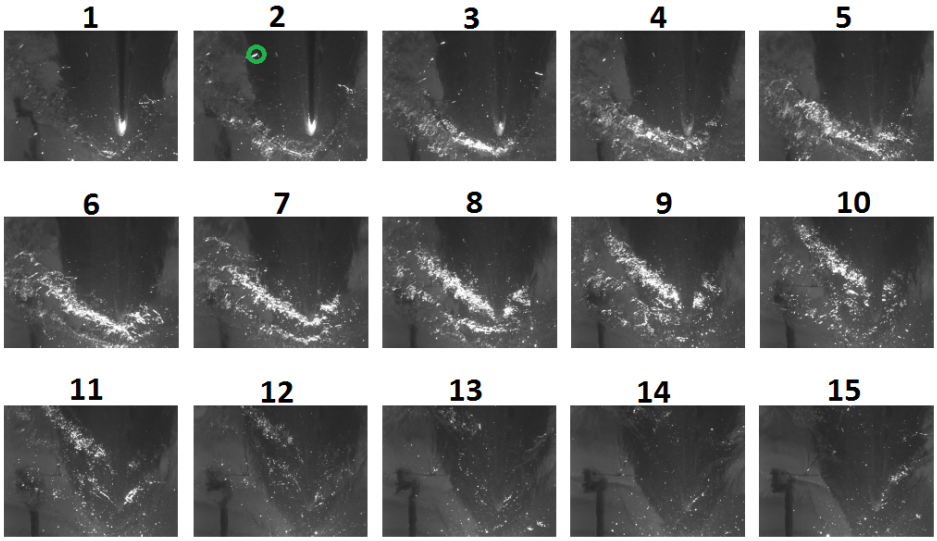

Figure 10: Images in the (y,z) plane from the cam1 for a wave period with bubbles. The probe's tips location is visible at instant 2 and evidenced by a green circle.

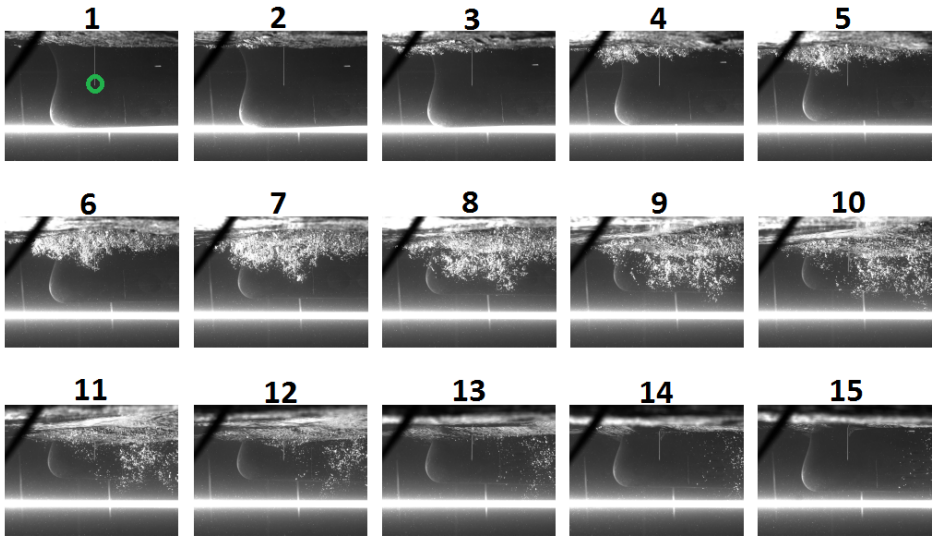

Figure 11: Images in the (x,z) plane from the cam2 for a wave period with bubbles.

3. Bubble detection by optical probe

Trials are conducted using the dual optical probe to measure, at a given position around the *Pp?* model, the bubble characteristics generated by breaking waves. The streamwise velocity and the diameter of the bubbles are the main parameters to characterize.

Figure 12 shows an example of the output voltage signal characteristic of a same bubble pierced by the two tips of the optical probe. In this figure, different parameters of the dewetting process are evidenced, that will be usefull in the following for processing the bubble size and velocity. The red signal corresponds to the upstream tip of the probe and the blue one to the downstream tip. The abscissa axis corresponds to the time in seconds and the ordinate axis corresponds to the output voltage signal of the optoelectronic module in volts. The calibration voltage under static condition in air (4.11 and $5.39V$ respectively for the upstream and downstream tips) is reached for tips fully dewetted.

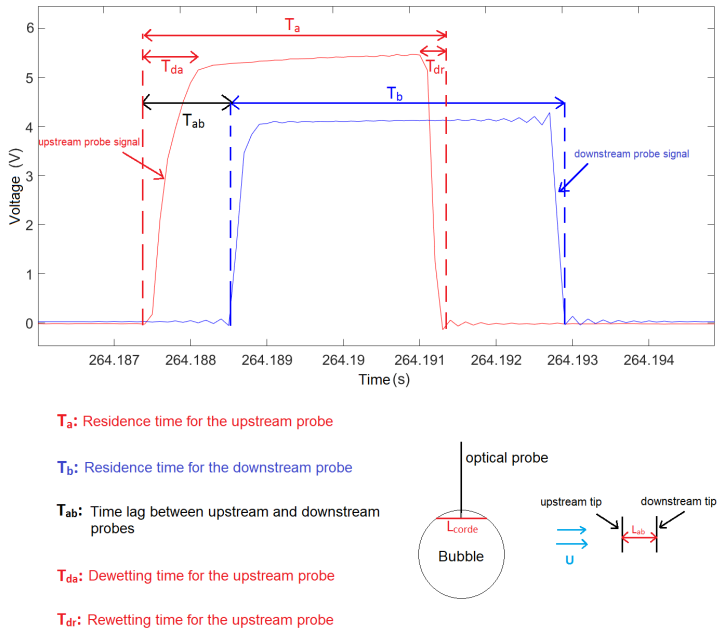

Figure 12: Example of output voltage characteristic of the dewetting of the two tips of the probe by a same bubble (associated bubble). Red curve : upstream tip, blue curve : downstream tip.

Each time the output voltage overcomes an imposed threshold value, the

tip of the probe is considered as being in the gas phase (g=1), otherwise it is in the liquid phase (g=0), where g denotes the instantaneous gas characteristic function. The same binarisation is applied to the voltage outputs of the two tips (threshold value defined here as 20% of the value expected in air for static conditions). The bubbles detection on the upstream tip allows to determine the local void fraction, ie: the averaged time fraction of the bubbles defined as $\alpha_a = \frac{\sum_i T_a(i)}{T}$, where i denotes the bubbles index and T is the measurement time. Due to the small size of the model, the measured local void fraction is very small: $\alpha_a = 0.003\%$. It is measured with a relative uncertainty of 9%. The detection of a same bubble on both tips (i.e. associated bubble) allows the calculation of the bubble's velocity, as well as the chord length of the bubble. The transit time (time lag noted T_{ab} in Figure 12) is defined as the difference between the times indicating the start of air detection between each tip of the probe. The time window used for T_{ab} for bubble association is $0.7ms < Tab < 15ms$. The bubble velocity obtained in the streamwise direction is $V_b = L_{ab}/T_{ab}$, where L_{ab} corresponds to the distance between the upstream and downstream tips of the probe (L_{ab} = 1,15 mm). The time window imposed for bubble association limits the bubble velocity that can be measured to the range of [0.08m/s-1.64m/s]. The validity of the relationship between V_b, T_{ab} and L_{ab} requires that the ratio of the transverse and normal velocity components to the streamwise velocity component remains much smaller than the ratio of the bubble size to the tips separation distance d_b/L_{ab}. This is obviously the case, when considering the mean velocity components of the flow induced by the sweep-down phenomenon measured by PIV in [Mallat et al. (2018a)]. In general, a bubble does not cross the tip by its center. So, the bubble is not expected to cut the tip along its diameter, but along a shorter length, which is called chord length L_c. The chord length L_c of each bubble was obtained as the product of the bubble velocity and its residence time T_a on the upstream tip ($L_c = V_b.T_a$). This allowed the determination of the distribution of the bubble chord length. Finally, we define a latency length representative of the size of the smaller gas structure that can be detected by the probe with complete dewetting of the probe. This length is the product of the interface velocity and the dewetting time T_{da} on the upstream tip ($L_{Latence} = V_b.T_{da}$). For saphire tips of $30\mu m$ in diameter, the latency length was characterized for a dewetting of the probe (liquid-air) by a plane interface with a controlled probe translation. For the

probe considered here, the latency length is 0.5 mm [Mäkiharju et al. (2013)]. Beyond an interface velocity of 0.2 m/s, the latency length is expected to be constant with regard to the interface velocity [Cartellier (1990)].

With the optical probe used in this work, each bubble velocity is determined with a relative uncertainty of ±16% and each bubble chord length is evaluated within ±29% of accuracy. These uncertainties include random error due to sampling at f_e and maximum systematic error induced by the voltage threshold application.

Table 2 summarizes the characteristics of the associated bubbles detected during the acquisition time. For each associated bubble, the time lag T_{ab}, the velocity V_b, the residence time on the upstream tip T_a, and the chord length L_{chord} are summarized. The averaged velocity of the bubbles is $0.81m/s \pm 0.026m/s$ and the averaged chord length is $4mm \pm 0.4mm$. The bubble velocity is plotted against the bubble chord length (see Figure 13). In the range [0.4m/s-1.4 m/s], the velocity does not depend on the chord length. It does not depend neither on the bubble size nor on the distance between the bubble center and the tip (which can lead to different bubble chord for same size). The plot of the bubble velocity versus the bubble residence time does not depict any trend of the bubbles velocity according to their residence time. This confirms that the piercing of the bubbles by the upstream tip does not affect noticeably the dynamics of the bubbles between the two tips and thus the measurement of the bubble's velocity. In addition, an examination of the anomalies of the piercing process for the measured extrema of the velocity, chord length, and residence time will be presented in the following.

Time(x10^6ms)	*Voltage(Volts)*		$T_{ab}(ms)$	$V_b(m/s)$	$T_a(ms)$	$L_c(mm)$	Extrema identified
	S_1	S_2			S_1	S_1	
0,2642	5,1	4	1	1,15	3,7	4,26	
0,297	5,2	4,0	1,6	0,7	7,6	5,5	
0,2971	4,6	4,1	0,9	1,3	2,9	3,7	
0,4654	5,1	4,2	2,4	0,5	7,0	3,4	
0,7901	5,4	4,0	3,1	0,4	4,5	1,7	
0,9419	2,0	4,2	1,4	0,8	0,7	0,6	
1,2330	5,2	4,0	1,2	1,0	5,1	4,9	
1,3160	5,2	4,0	2,2	0,5	11,2	5,9	
1,3161	1,8	0,8	1,5	0,76	0,1	0,08	B_3
1,6110	4,0	4,0	1,5	0,8	1,1	0,8	
1,6880	5,1	4,1	1,6	0,7	4,6	3,3	
1,9784	5,0	4,0	1,3	0,9	2,3	2,0	
1,9784	5,4	4,0	1,0	1,2	3,7	4,3	
1,9785	5,2	4,0	1,2	1,0	11,1	10,6	
2,1336	5,0	3,9	8,7	0,12	0,9	0,13	B_2
2,2146	5,3	4,0	1,6	0,7	7,8	5,6	
2,3653	5,2	4,0	1,7	0,7	7,4	5,0	
2,5842	5,3	4,0	2,2	0,5	7,7	4,0	
2,5856	5,2	4,0	1,1	1,0	2,3	2,4	
2,5983	5,1	3,2	2,3	0,5	1,6	0,8	
2,7200	5,1	4,0	1,8	0,6	10,2	6,5	
2,7570	3,1	3,8	1,1	1,0	0,8	0,8	
3,0190	5,1	4,0	1,8	0,6	1,2	0,8	
3,1670	5,3	4,0	0,9	1,3	3,4	4,3	
3,2870	5,4	4,0	0,8	1,43	12,3	17,7	B_1

Table 2: Summary of some associated bubble characteristics.

Extrema of the bubble velocity are identified in Figure 13 (B_1: $L_c = 17.7mm$, $V_b = 1.4m/s$ and B_2 : $L_c = 0.12mm$, $V_b = 0.13m/s$); they correspond to the extrema of the bubble's chord length. B_1 is also characterized by a maximum value of the residence time. The corresponding output voltage of these two bubbles is displayed in Figure 14. As can be seen, there is no anomaly in the dewetting of the tips and no ambiguity for the association of the bubble on the two tips for these two cases.

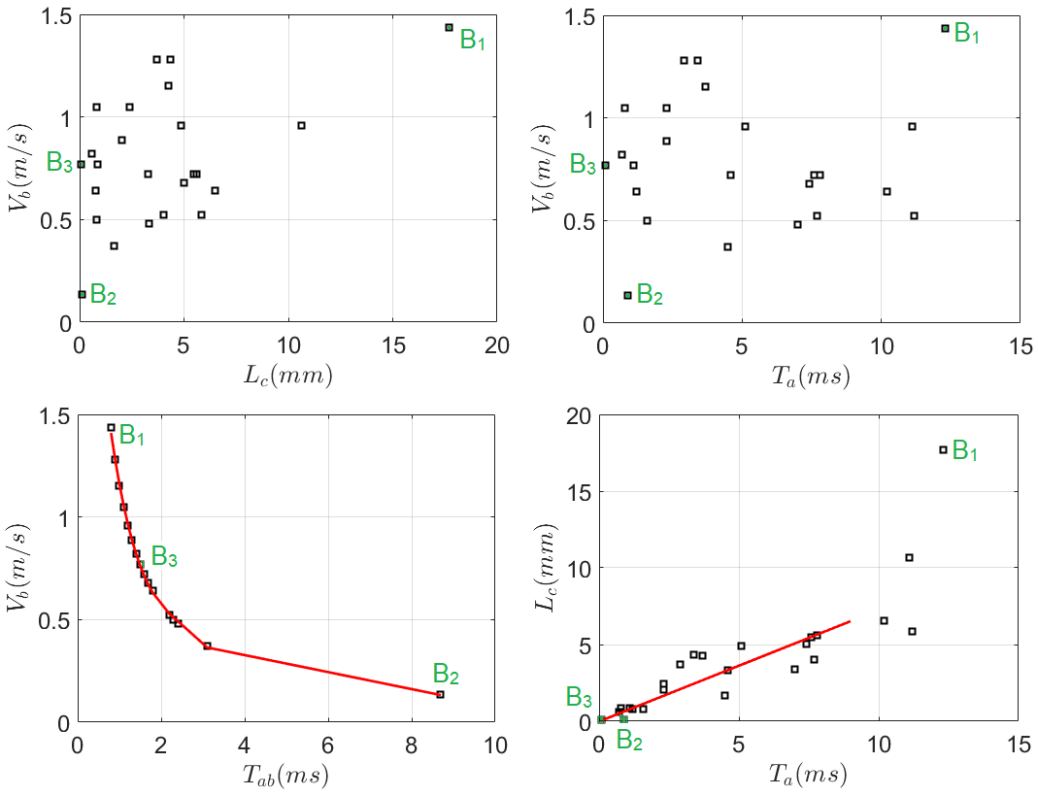

Figure 13: Characteristics of some detected bubbles.

Another case of extremum of the bubble chord length is highlighted with B_3, characterized by a minimum of the residence time (B_3: $L_c = 0.08mm$, $V_b = 0.76m/s$). The corresponding output signal is depicted in Figure 14, showing an example of partial dewetting of the two tips. It is either due to a size of the bubble smaller than the latency length or to a trajectory of the bubble that makes it cross the tips far from the bubble's axis. Partial dewetting is not a problem for the characterization of bubble chord length and velocity, as much as there is no ambiguity for the association of the bubble on the two tips, which is obviously verified here. Consequently, the analysis of the voltage outputs of all associated bubbles have revealed no anomaly in the measurement. Therefore, large chord length above 10mm are obviously attributed to bubbles coalescence. Among the four phenomena that can be responsible for coalescence, identified by [Liao and Lucas (2010)], the best candidates are: 1) random collisions due to the turbulence induced

by the breaking wave and bubble sweep-down phenomenon, and 2) wake entrainment. Figure 15 illustrates the entrainment of two bubbles in the wake of a first one. Bubbles entrapped in the wake are characterized by larger streamwise velocity. The third bubble is obviously the consequence of coalescence.

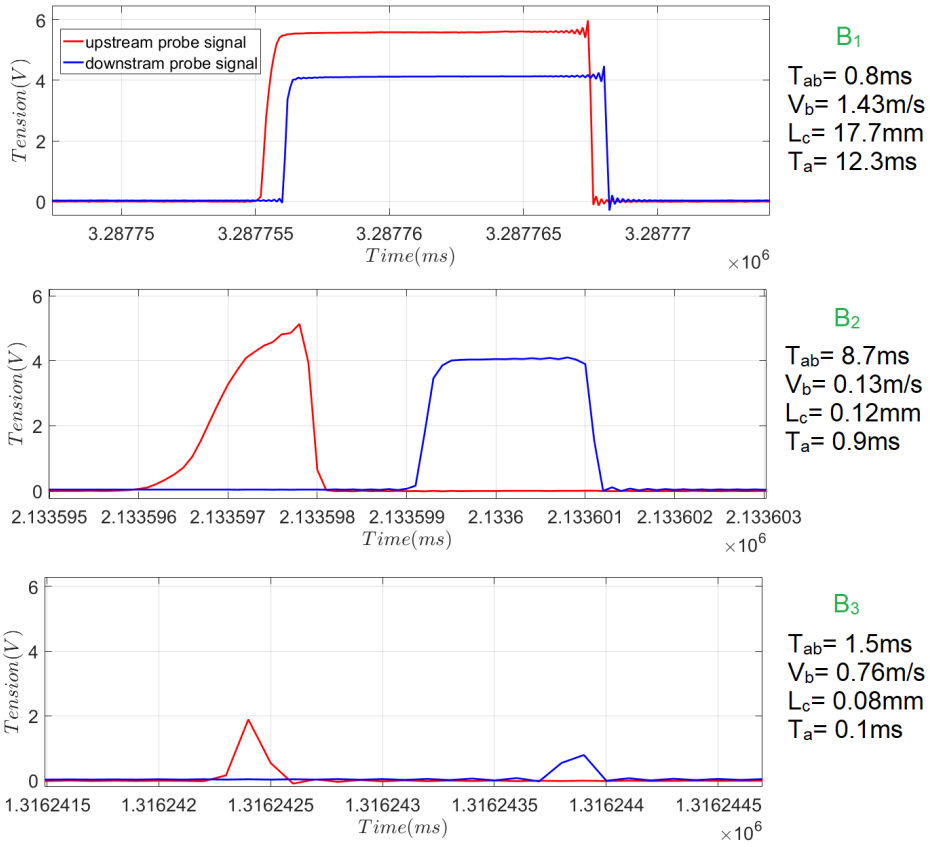

Figure 14: Example of voltage output for extrema of the bubble velocities and chord lengths. Red curve : upstream tip, blue curve : downstream tip.

Figure 13 shows the evolution of the chord length of the bubbles with regard to their residence time. The best linear fit, obtained when coalesced bubbles of chord length larger than 10mm are suppressed from the analysis, is also displayed on this Figure. It corresponds to a fitted bubble streamwise velocity $V_{bfit} = 0.72m/s$. Figure 16 shows the % of total associated bubbles according to their chord lengths and velocities.

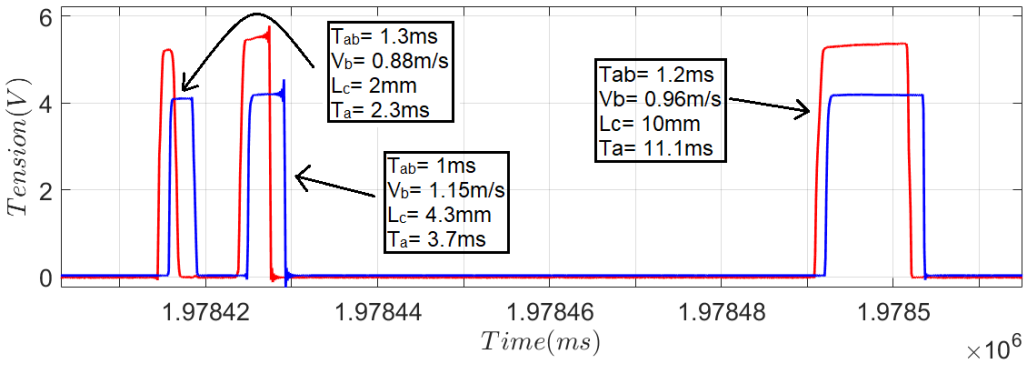

Figure 15: Example of bubbles output voltage events that shows in the wake of each other, and coalescence.

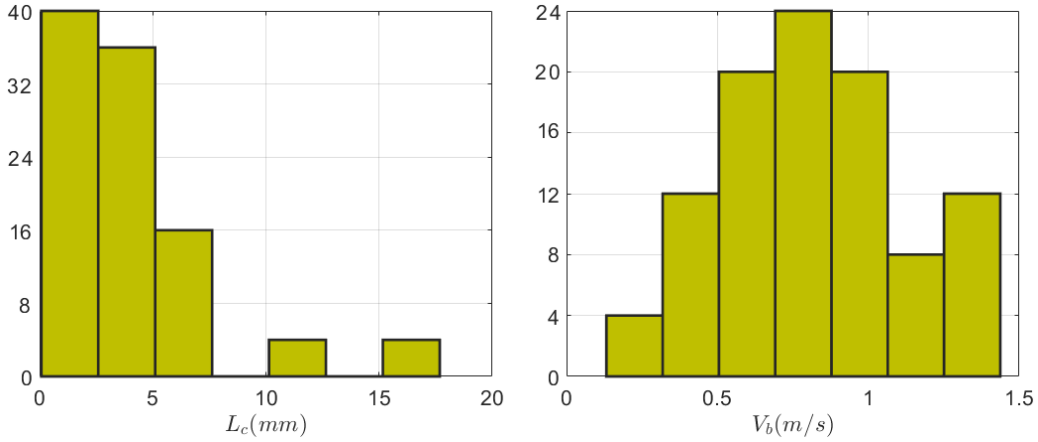

Figure 16: Histograms of total associated bubbles in % according to their chord lengths and velocities.

The results show that the bubbles detected following the breaking bow wave around the model have velocities that vary between 0.1 and 1.4m/s, with an important number of bubbles having a 0.8 m/s velocity. Thus, the average bubble velocity is of the order of the current velocity, which confirms that at this location of the flow, the bubbles are mainly carried away by the current without drift. Regarding the bubble sizes, we identify small bubbles of some mm of chord length as we identify big bubbles of up to 17mm in chord length. When bubbles of chord length larger than 10 mm, generated by coalescence, are removed from the statistical analysis, the ensemble averaged chord length is 3.1mm ($L_{c_{mean}}$). Assuming that the shape of uncoalesced

bubbles is spherical, the ensemble averaged diameter can be deduced from the average chord length, following the formulation of [van Gils et al. (2013)]: $db_{mean} = 1.5 \times L_{c_{mean}}$. Thus, from measurements with the optical probe, it is expected at the location of the probe millimetric bubbles with a mean diameter of 4.6mm, and centimetric non spherical coalesced bubbles.

4. Bubble characterization by image processing

Another method to determine bubble velocity and size is also developed. This method is based on the detection of individual bubbles in the (x,z) plane on pairs of raw images acquired with the PIV camera and on the use of a custom made algorithm of Tracking Velocimetry. This method provides additional data to that given by the optical probe. In particular, it can provide further information such as the vertical velocity components of the bubbles, trapped and advected around the ship bow. Figure 17 shows an example of a raw image with bubbles (a). The field of view is (528x396) mm^2 for (1600x1200) pixel x pixel. After binarisation of the intensity of the image, contours of the bright objects are identified (in blue) (b). Different intensity thresholds were tested in order to detect the bubbles contours accurately and it was shown that the threshold variations have very little influence on the results presented in the following. A mask is applied on the free surface and the laser sheet [Dussol et al. (2016))]. The centroid coordinates of all exploitable bubbles are determined (c).

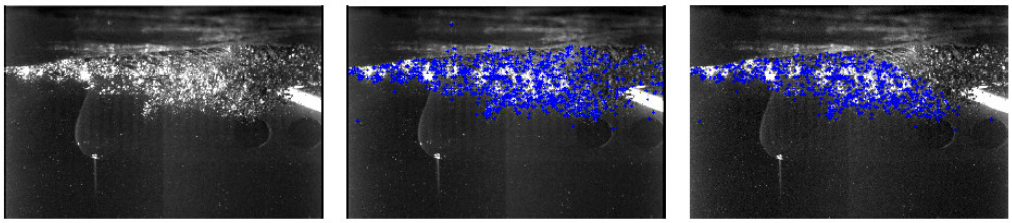

Figure 17: (a): Raw image, (b): Bubbles gravity center detection (blue dots), (c): Applying a mask at the level of the free surface and the laser sheet.

Based on their contours, the apparent areas of the bubbles are calculated and the coordinates of the gravity center of the bubbles are determined. The equivalent diameter is obtained from the bubble apparent area, assuming spherical shape. Due to both the spatial resolution of the optical set-up

and the subpixel resolution of the procedure, the uncertainty on the determination of the bubble equivalent diameter is $\pm 0.48 pixel$ (ie : $\pm 0.16 mm$) and the uncertainty on the positioning of bubble's centroidis $\pm 0.12 pixel$ (ie : $\pm 39 \mu m$) The bubble's velocity is calculated by analyzing the displacement of each bubble centroid between two consecutive images in a same pair of images. This involves defining a bubble displacement window based on previous PIV measurements of seeding particles in the flow under the same conditions [Mallat et al. (2018b)] where the instantaneous velocity vector fields have been obtained using an Adaptive PIV algorithm with an interrogation window size of 32 x 32 $pixels^2$ and an adjacent windows of 25% overlapped. These PIV measurements showed that the velocity components of seeding particles were 0.75m/s and 0.3m/s respectively. Between two images of a same pair corresponding to a time between pulse of $dt = 1200 \mu s$, the displacement of seeding particles in the flow (corresponding to the mean velocity of the flow) was therefore of the order of 3 pixels along the horizontal axis and 1.5 pixels along the vertical axis. The bubble displacement window intervals between 2 consecutive images are then defined between 0 and +6 pixels in the streamwise direction and between -4 and +4 pixels vertically (see Figure 18). This corresponds to a bubble velocity limit of 1.5m/s along the horizontal axis and $\pm 0.8 m/s$ along the vertical axis. This interval is used to identify a same bubble on two consecutive images of a pair. The bubble velocities are calculated locally by analyzing the displacement of each bubble successively. The algorithm associates the bubble on the image (b) from the coordinates of the bubble centroids of the image (a) as shown in Figure 17. The bubbles velocity component are then calculated from the coordinates of the two successive positions of an associated bubble and from the time step dt between the images of a pair. This gives rise to an uncertainty on the determination of the bubbles velocity component of $\pm 0.066 m/s$, due to the sub-pixel resolution of the bubbles centroid positioning. The calculation of bubble velocities is averaged over a measurement time of $180 s$ with an acquisition rate of the images pairs of $8.5 Hz$. Taking into account the statistical convergence of the different measured quantities, the results show that the mean longitudinal and vertical bubble velocities are of the order of $0.5 \pm 0.15 m/s$ and $-0.13 \pm 0.02 m/s$ respectively. Regarding their size, the diameter of the detected bubbles varies between 0.7 and 5mm. The mean diameter is of the order of $3.0 \pm 0.6 mm$.

This method for the determination of the velocity of individual bubbles is reliable if: (1) the bubbles are small enough to avoid deformability, (2) few

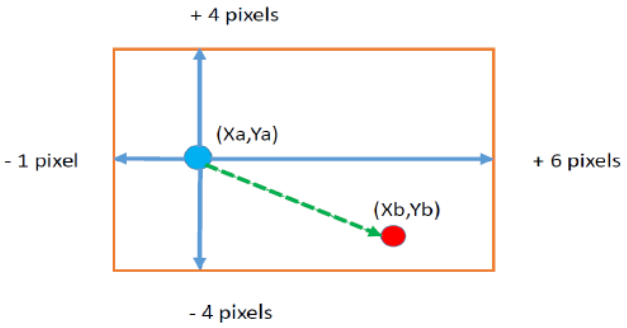

Figure 18: The bubble displacement window for the detection of the bubble (Xb; Yb) on the image (2) from the coordinates of the bubble (Xa; Ya) on the image (a).

bubbles are superimposed in the depth of field and (3) the displacement of the bubbles centroid during the time step of an images pair is smaller than the bubble's equivalent diameter. Condition (3) is obviously verified.

However, the detection of bubbles between two PIV images of a pair is not 100% effective. Figure 19 shows a zoom on a pair of images (Images 1 and 2). Bubble centers were marked by blue dots and a red circle when these are detected on the second picture. Due to bubbles superimposition in the depth of field (y direction), a bubble "split" can be seen between two consecutive images, as well as the presence of bubbles detected on image (2) that are not detected on Image (1). Therefore, there can be several problems such as geometric deformation, and splitting and merging of bubbles between the two images. These phenomena limit the rate of associated bubbles between two consecutive images into an images pair to 90% of the total number of detected bubbles.

The two bubble characterization methods (optical probe and visualization of raw images and image processing) are reliable. However, the use of optical probe has the advantage of knowing the position of the bubble in three dimensions of space, which is not the case for the visualization method. For the latter, bubbles velocity and diameter are averaged over the thickness of the bubble cloud in the y direction. This could explain the difference between the results obtained by the two methods. The bubble detection by optical probe allows to access to some particular characteristics of the bubbles, especially their local velocity and the local averaged diameter. This type of intrusive and punctual measure provides complementary analysis with 2D and 3D previous studies to characterize the bubble sweep-down phenomenon

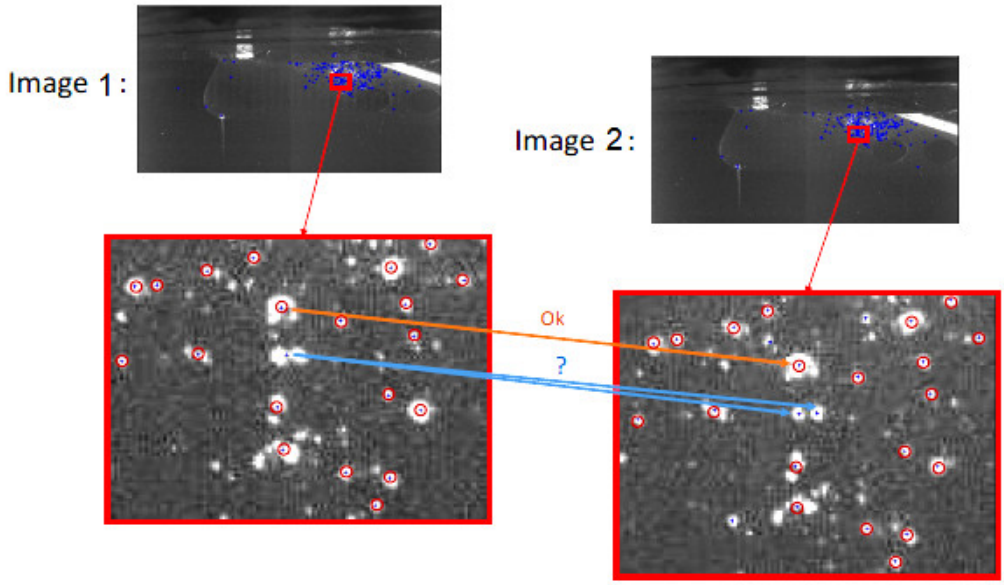

Figure 19: Visualization of the bubble detection on both images 1 and 2.

around the ship model.

5. The bubbles characteristics at small and real scales

With the Froude similitude, the ratio of the velocity of the plunging jet of the bow wave $U_{plungingjet}$ to the current velocity $U_{current}$ is preserved between the model and the ship at full scale, and so is expected for the ratio of the bubble velocity components to the current velocity for the different scales : $(\frac{U_b}{U_{current}})_{model} \approx (\frac{U_b}{U_{current}})_{fullscale}$. The bubble size can be roughly estimated by considering that for bubbles entrapped under the free surface, the velocity of the plunging jet must overcome their terminal rising velocity achieved in the viscous fluid at rest. This yields to the following relationship for the scaling of the bubble size : $d_b \sim \sqrt{\frac{\nu}{g}\frac{U_{plungingjet}}{U_{current}}U_{current}}$. With the Froude similitude, this leads to the following ratios of the bubble size for the model and at full scale: $(\frac{d_b}{L_{pp}})_{model} \sim K^{-3/4}(\frac{d_b}{L_{pp}})_{fullscale} \approx 13(\frac{d_b}{L_{pp}})_{fullscale}$, ie: $(d_b)_{model} \approx 0.4(d_b)_{fullscale}$. Here, K is the scale factor between the model and

the real ship: $K = \frac{(L_{pp})_{model}}{(L_{pp})_{fullscsale}} = \frac{1}{30}$ As discussed in the work of [Waniewski et al. (2001)], the air flow rate entrapped by the bow wave can be scaled by the following model, with $d_{plungingjet}, L_{plungingjet}$ being the diameter and length of the plunging jet and β being the impingement angle of the jet: $Q_{air}(m^3/s) \sim 0.21\frac{d^{3/2}_{plungingjet} L^{1/3}_{plungingjet} U^2_{plungingjet}}{sin\beta}$. By assuming similitude of the Froude number, the ratios of the characteristic lengths of the bow wave to the ship length is preserved, as well as the impinging angle and so is expected for the ratio of the characteristic lengths of the plunging jet to the ship length. This implies that scale factor effect on the volume of air entrapped in the bubbles clouds is: $\frac{(Q_{air})_{model}}{(Q_{air})_{fullscale}} \sim K^{17/6} \approx 6 \times 10^{-5}$. Here, K is the scale factor between the model and the real ship: $K = \frac{(L_{pp})_{model}}{(L_{pp})_{fullscsale}} = \frac{1}{30}$. For small void fractions, the air volume fraction is equivalent to the air flow rate divided by the water flow rate and it can be scaled with: $\alpha \sim \frac{Q_{air}}{U_{current} L^2_{pp}} \sim \frac{Q_{air}}{Frg^{1/2} L^{5/2}_{pp}}$. With the Froude similitude, this involves a scale factor effect on the void fraction, which can be modelized by the following relationship: $\frac{(\alpha)_{model}}{(\alpha)_{fullscale}} \sim K^{1/3} \approx 0.33$. The void fraction for the model, which has been determined based on the use of the optical probe, is representative of the fraction of the total air residence time over the total measurement time T. Now if we focus on the residence time of the bubbles clouds during each wave period $T_c \approx 0.25s$, we can evaluate the average void fraction α_c inside the bubbles clouds as: $\alpha_c = \frac{\alpha}{fT_c} \approx 0.014\%$; f being the wave frequency in the tank. Based on the measurements achieved in the flume tank around the bow of the *Pp?*'s model, it is possible to have an estimation of the expected bubbles size, and void fraction expected around the bow of the *Pp?* at full scale. For the real size and conditions of the trial at sea, we expect big centimetric bubbles, and a local void fraction in the bubbles clouds of $\alpha_c \approx 0.04\%$. In the context of oceanographic and research vessels, the bubble size and the void fraction are important parameters as they influence the transmission of the acoustic waves through the bubbles clouds along the hull. In particular, the resonant frequency of the bubbles, which is directly

linked to the bubble size, is the main parameter to know in order to optimize the bandwidth of the acoustic transducers.

6. Conclusion

Despite the complexity of the bubble sweep-down phenomenon, the results of recent 3D characterization of bubble clouds around a 1/30 scale ship model of the *Pp?* helped to improve our knowledge of the generation and propagation process of bubble clouds around the bow. Based on these results, additional complementary tests are carried out to investigate some interesting characteristics of individual bubbles that are trapped within the clouds.

Using an optical probe, the time averaged gas fraction and statistics of the size and the velocity of the bubbles around the hull of ship, have been measured locally. The probe has been immersed at a location along the trajectory of bubble clouds. The results obtained showed that bubbles of mean diameter 4.6mm coexist with centimetric coalesced bubbles. At the location of the probe (i.e. 250 mm from the symmetrical axis of the bow), the bubbles mean streamwise velocity is of the order of 0.8m/s which corresponds to the current velocity.

Another method for the characterization of the bubbles, based on the detection of bubbles on raw images, have been developed. The results show that the mean streamwise and vertical downward bubbles velocities are of the order of 0.5m/s and -0.13m/s respectively. Regarding the size of bubbles, the mean diameter of the bubbles detected is of the order of 3mm. Bubbles velocity and size deduced from visualizations are integrated over the clouds thickness. The two methods give interesting results.

From an acoustical survey problematic point of view, the knowledge of the bubbles sizes and void fraction is necessary as it influences the diffusion and extinction volumetric cross section. Even if scale effects are significant and the results in term of bubble size and void fraction are not the same in the flume tank and at real scale, this study allows the quantification of the bubble sweep-down phenomenon around the bow of the ship under waves and current. In addition, it gives access to some particularly interesting characteristics of bubbles entrapped along the ship hull. The overall results provide an interesting complementary experimental database which could be used for the validation of future numerical models.

Acknowledgements

The authors would like to thank Ifremer and the Hauts-de-France Regional Council for the financial funding of the PhD project. We are also grateful to Thomas Bacchetti, Jean-Valery Facq and Benoit Gaurier for their assistance in the design and set-up of these experiments.

References

J. Dalen, A. Lovik, The influence of wind-induced bubbles on echo integration surveys, The Journal of the Acoustical Society of America 69 (1981) 1653–1659.

C.-y. Guo, P. Xu, W. Wang, Y. Han, Y.-f. Kuai, Y.-w. Fan, Experimental study on bubble sweep-down characteristics of research vessels, Ocean Engineering 228 (2021) 108963.

B. Mallat, G. Germain, J.-Y. Billard, B. Gaurier, A 3d study of the bubble sweep-down phenomenon around a 1/30 scale ship model, European Journal of Mechanics-B/Fluids 72 (2018a) 471–484.

B. Mallat, G. Germain, B. Gaurier, P. Druault, J.-Y. Billard, Experimental study of the bubble sweep-down phenomenon on three bow designs, Ocean Engineering 148 (2018b) 361–375.

S. Delacroix, G. Germain, L. Berger, J.-Y. Billard, Bubble sweep-down occurrence characterization on research vessels, Ocean Engineering 111 (2016) 34–42.

F. W. Shabangu, E. Ona, D. Yemane, Measurements of acoustic attenuation at 38 khz by wind-induced air bubbles with suggested correction factors for hull-mounted transducers, Fisheries research 151 (2014) 47–56.

J. Li, A. Castro, P. Carrica, Progress on prediction of bubbly flows around ships, in: Fluids Engineering Division Summer Meeting, volume 50299, American Society of Mechanical Engineers, 2016, p. V01BT30A001.

F. Moraga, P. Carrica, D. Drew, R. Lahey Jr, A sub-grid air entrainment model for breaking bow waves and naval surface ships, Computers & Fluids 37 (2008) 281–298.

J. Song, L. Bian, E. Yang, D. Su, Bubble density gradient with laser detection: A wake-homing scheme for supercavitating vehicles, Advances in Mechanical Engineering 10 (2018) 1687814018782345.

J. P. Johansen, A. M. Castro, P. M. Carrica, Full-scale two-phase flow measurements on athena research vessel, International journal of multiphase flow 36 (2010) 720–737.

F. Noblesse, G. Delhommeau, M. Guilbaud, D. Hendrix, C. Yang, Simple analytical relations for ship bow waves, Journal of Fluid Mechanics 600 (2008) 105–132.

F. Noblesse, G. Delhommeau, L. Hua, D.-c. Wan, Y. Chi, Ship bow waves, Journal of Hydrodynamics, Ser. B 25 (2013) 491–501.

G. Delhommeau, M. Guilbaud, L. David, C. Yang, F. Noblesse, Boundary between unsteady and overturning ship bow wave regimes, Journal of Fluid Mechanics 620 (2009) 167–175.

S. Delacroix, G. Germain, B. Gaurier, J.-Y. Billard, Experimental study of bubble sweep-down in wave and current circulating tank: Part i—experimental set-up and observed phenomena, Ocean Engineering 120 (2016) 78–87.

H. Medwin, Counting bubbles acoustically: a review, Ultrasonics 15 (1977) 7–13.

S. A. Thorpe, On the clouds of bubbles formed by breaking wind-waves in deep water, and their role in air-sea gas transfer, Philosophical Transactions of the Royal Society of London. Series A, Mathematical and Physical Sciences 304 (1982) 155–210.

V. Akulichev, V. Bulanov, S. Klenin, Acoustic sensing of gas bubbles in the ocean medium, Soviet Physics. Acoustics 32 (1986) 177–180.

E. J. Terrill, W. K. Melville, A broadband acoustic technique for measuring bubble size distributions: Laboratory and shallow water measurements, Journal of atmospheric and oceanic technology 17 (2000) 220–239.

M. Abbaszadeh, M. M. Alishahi, H. Emdad, Experimental investigations on the bubbly wake of a transom stern model using optical laser beam scattering characteristics, Applied Ocean Research 104 (2020) 102380.

M. V. Trevorrow, S. Vagle, D. M. Farmer, Acoustical measurements of microbubbles within ship wakes, The Journal of the Acoustical Society of America 95 (1994) 1922–1930.

S. Vagle, H. Burch, Acoustic measurements of the sound-speed profile in the bubbly wake formed by a small motor boat, The Journal of the Acoustical Society of America 117 (2005) 153–163.

S. Stanic, E. Kennedy, B. Brown, D. Malley, R. Goodman, J. Caruthers, Broadband acoustic transmission measurements in surface ship wakes, in: OCEANS 2007, IEEE, 2007, pp. 1–10.

M. Birvalski, R. Boucheron, M. van Rijsbergen, D. Frechou, Developments in micro-bubble measurement techniques for cavitation and piv experiments, in: Sixth International Conference on Advanced Model Measurement Technology for the Maritime Industry (AMT'19), Rome, Italy, 2019.

M. Birvalski, M. X. van Rijsbergen, Application of interferometric particle imaging to cavitation nuclei measurements in a ship model basin, in: Proceedings of the 19th 2018 international symposium on the application of laser and imaging techniques to fluid mechanics, Lisbon, 2018.

D. Lebrun, D. Allano, F. Walle, F. Corbin, L. Méès, D. Fréchou, R. Boucheron, Size nuclei measurement in a cavitation tunnel by digital in-line holography, in: 2nd International Conference on Advanced Model Measurement Technology for EU Maritime Industry (AMT'11), 2011.

D. Lebrun, D. Allano, F. Walle, Y. Lecoffre, R. Boucheron, D. Fréchou, et al., Development of interferometric techniques for nuclei size measurement in cavitation tunnel, in: 28th Symposium on Naval Hydrodynamics, 2010.

R. Van der Welle, Void fraction, bubble velocity and bubble size in two-phase flow, International journal of multiphase flow 11 (1985) 317–345.

S. Ceccio, D. George, A review of electrical impedance techniques for the measurement of multiphase flows (1996).

D. L. George, C. O. Iyer, S. L. Ceccio, Measurement of the bubbly flow beneath partial attached cavities using electrical impedance probes, J. Fluids Eng. 122 (2000) 151–155.

T. A. York, Status of electrical tomography in industrial applications, Journal of Electronic imaging 10 (2001) 608–619.

D. S. Holder, Electrical impedance tomography: methods, history and applications, CRC Press, 2004.

B. R. Elbing, E. S. Winkel, K. A. Lay, S. L. Ceccio, D. R. Dowling, M. Perlin, Bubble-induced skin-friction drag reduction and the abrupt transition to air-layer drag reduction, Journal of Fluid Mechanics 612 (2008) 201–236.

B. Stutz, S. Legoupil, X-ray measurements within unsteady cavitation, Experiments in fluids 35 (2003) 130–138.

O. Coutier-Delgosha, B. Stutz, A. Vabre, S. Legoupil, Analysis of cavitating flow structure by experimental and numerical investigations, Journal of Fluid Mechanics 578 (2007) 171–222.

W. Hassan, S. Legoupil, D. Chambellan, S. Barre, Dynamic localization of vapor fraction in turbo pump inducers by x-ray tomography, IEEE Transactions on Nuclear Science 55 (2008) 656–661.

V. Aeschlimann, S. Barre, S. Legoupil, X-ray attenuation measurements in a cavitating mixing layer for instantaneous two-dimensional void ratio determination, Physics of Fluids 23 (2011) 055101.

S. A. Mäkiharju, C. Gabillet, B.-G. Paik, N. A. Chang, M. Perlin, S. L. Ceccio, Time-resolved two-dimensional x-ray densitometry of a two-phase flow downstream of a ventilated cavity, Experiments in fluids 54 (2013) 1–21.

A. Cartellier, Optical probes for local void fraction measurements: characterization of performance, Review of Scientific Instruments 61 (1990) 874–886.

Y. Liao, D. Lucas, A literature review on mechanisms and models for the coalescence process of fluid particles, Chemical Engineering Science 65 (2010) 2851–2864.

D. P. van Gils, D. N. Guzman, C. Sun, D. Lohse, The importance of bubble deformability for strong drag reduction in bubbly turbulent taylor–couette flow, Journal of fluid mechanics 722 (2013) 317–347.

D. Dussol, P. Druault, B. Mallat, S. Delacroix, G. Germain, Automatic dynamic mask extraction for piv images containing an unsteady interface, bubbles, and a moving structure, Comptes Rendus Mécanique 344 (2016) 464–478.

T. Waniewski, C. Brennen, F. Raichlen, Measurements of air entrainment by bow waves, J. Fluids Eng. 123 (2001) 57–63.